

Title	Conical shear-driven parametric instability of steady flow in precessing spheroids
Author(s)	Horimoto, Yasufumi; Katayama, Atsushi; Goto, Susumu
Citation	Physical Review Fluids. 2020, 5(6), p. 063901
Version Type	VoR
URL	https://hdl.handle.net/11094/100044
rights	Copyright 2020 by the American Physical Society
Note	

Osaka University Knowledge Archive : OUKA


<https://ir.library.osaka-u.ac.jp/>

Osaka University

Conical shear-driven parametric instability of steady flow in precessing spheroids

Yasufumi Horimoto ^{*}

*Faculty of Science and Engineering, Tokyo University of Science, 2641 Yamazaki,
Noda, Chiba 278-8510, Japan*

Atsushi Katayama and Susumu Goto [†]

*Graduate School of Engineering Science, Osaka University, 1-3 Machikaneyama,
Toyonaka, Osaka 560-8531, Japan*



(Received 5 December 2019; accepted 19 May 2020; published 16 June 2020)

We investigate experimentally the instability of steady flow of fluid confined in weakly precessing spheroids. It is known that the conical-shear instability (CSI) proposed by Lin, Marti, and Noir [*Phys. Fluids* **27**, 046601 (2015)] grows in a precessing sphere, and the elliptical and shearing instabilities [Kerswell, *Geophys. Astrophys. Fluid Dyn.* **72**, 107 (1993)] can grow in precessing spheroids. Previous theories predict that when $\text{Re} \lesssim \eta^{-5}$, where Re is the Reynolds number defined by the spin angular velocity and the equatorial radius of the spheroid and η is its ellipticity, CSI dominates the other two instabilities even in a spheroid, and that, in particular, when $\eta < 0.17$ the critical Poincaré number (i.e., the critical precession rate) $\text{Po}^{(c)}$ is proportional to $\text{Re}^{-3/10}$ for $200\eta^{-2} \ll \text{Re} \lesssim \eta^{-5}$. To experimentally verify these predictions, we measure a long time-series of fluid velocity to accurately estimate the power spectrum. Then, we determine $\text{Po}^{(c)}$ as a function of Re and show the qualitative change of its scaling depending on η . Our experimental results perfectly support the theoretical predictions, implying that CSI can grow in precessing spheroids.

DOI: [10.1103/PhysRevFluids.5.063901](https://doi.org/10.1103/PhysRevFluids.5.063901)

I. INTRODUCTION

In a container rotating at a constant angular velocity $\boldsymbol{\Omega}_s$, the flow of a confined viscous fluid always tends to solid-body rotation at $\boldsymbol{\Omega}_s$ irrespective of the initial conditions and of the container shape. Therefore, the sustainment of a nontrivial flow of confined fluid requires a time-dependent rotation of the container. One method is to change the sign or magnitude Ω_s of the angular velocity $\boldsymbol{\Omega}_s$ in time. Another, and more efficient, method is to change the direction $\boldsymbol{\Omega}_s/\Omega_s$ ($=\hat{\mathbf{z}}$) of the rotational axis. The precession (Fig. 1) is this kind of motion. More precisely, it is the rotation of the spin axis $\hat{\mathbf{z}}$ itself with an angular velocity $\boldsymbol{\Omega}_p$ about another axis (the precession axis). In the present study, we only consider the case in which $\boldsymbol{\Omega}_p$ is perpendicular to $\boldsymbol{\Omega}_s$. It is known that the precession of a container realizes a surprising variety of flows of confined fluid. In particular, the fact that a weak precession sustains fully developed turbulence has been attracting the attention of researchers in many fields (see a review by Le Bars *et al.* [1] and other references [2–19]).

^{*}horimoto@rs.tus.ac.jp

[†]goto@me.es.osaka-u.ac.jp

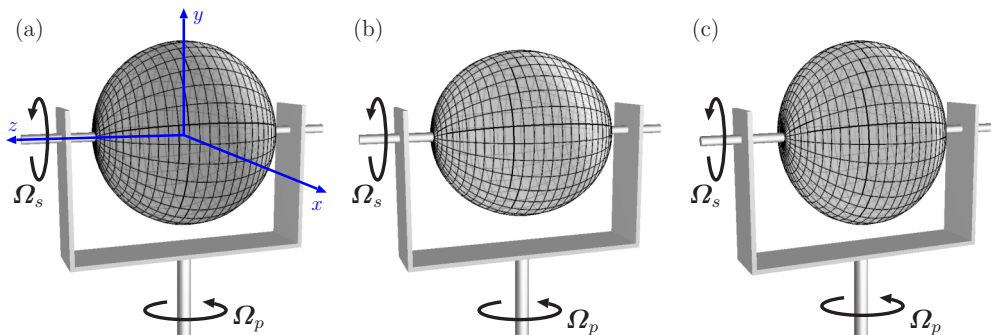


FIG. 1. Three precessing containers used in the experiments: (a) sphere ($\eta = 0$), (b) prolate spheroid ($\eta = -1/9$), and (c) oblate spheroid ($\eta = 1/10$). Precession frame (x, y, z) defined as in (a) rotates at Ω_p with respect to the laboratory frame. We consider the case in which $\Omega_p \perp \Omega_s$.

The most important control parameter of the precession-driven flow is the Poincaré number,

$$\text{Po} = \frac{\Omega_p}{\Omega_s} \quad (\Omega_p = |\Omega_p|), \quad (1)$$

which indicates the magnitude of the precession. On the other hand, the Reynolds number,

$$\text{Re} = \frac{a^2 \Omega_s}{\nu}, \quad (2)$$

or the Ekman number, $\text{Ek} = \text{Re}^{-1}$, defined in terms of Ω_s , the kinematic viscosity ν of the confined fluid, and the dimension a of the container (e.g., the equatorial radius of a spheroid), is the indicator of the spin rate. It is a fundamental question how the flow state in a precessing container changes as Po increases for a fixed Re . Previous studies showed that when Po is sufficiently small, the flow is steady in the precession frame, which rotates at Ω_p with respect to the laboratory frame. Then, as Po increases, the steady flow becomes unstable to bifurcate to periodic flow and then to turbulence. Stronger rotation [say, $\text{Po} = O(1)$], however, leads to laminarization because the precession axis Ω_p/Ω_p is stationary in the laboratory frame. It is therefore important to determine the first bifurcation point, namely the critical Poincaré number $\text{Po}^{(c)}$ as a function of Re and the container shape. This is the main purpose of the present experimental study. Namely, we determine experimentally $\text{Po}^{(c)}$ for the flow in precessing spheroids with a small ellipticity,

$$\eta = \frac{a - b}{a} \quad (3)$$

(where a and b denote the equatorial radius and polar radius of a spheroidal container, respectively; see Fig. 1), in a moderate Re range ($\lesssim 10^5$).

We emphasize that this is a nontrivial problem because, as is well described by Lin *et al.* [20] and summarized in the next section, there are three possible instabilities of the steady flow driven by precession, namely elliptical instability, shearing instability, and conical-shear instability (CSI). The former two instabilities are due to the ellipticity of a spheroidal container, and they were analyzed in detail by Kerswell [21,22]; see also a recent review by Le Bars *et al.* [1]. The asymmetry of the container distorts streamlines of the solid-body rotational flow of the confined fluid and leads to these instabilities. The elliptical instability is due to the distortion of each circular streamline, while the shearing instability grows when the line consisting of the centers of the streamlines is not perpendicular to the circulation planes. On the other hand, CSI was recently proposed by Lin *et al.* [20]. The boundary-layer equations on precessing spheroidal and spherical cavity walls have singular points at certain latitudes [23–26], and conical shear layers are spawned into a bulk region

from these latitudes forming annulus regions [25,26]. These shear layers are reported by many numerical simulations [20,27–31], and, for a spherical geometry, Kida [26] analytically derived their explicit expression. CSI grows in these conical shear layers. All of the above instabilities grow due to a resonance of unstable modes and a base flow rotating about an inclined axis with respect to the spin axis.

For $\eta = 0$ (i.e., a precessing sphere) only CSI, rather than the other two instabilities, grows. The stability of steady flow for the sphere has been investigated by experimental, numerical, and theoretical approaches. Goto *et al.* [11] conducted flow visualization on the steady-unsteady transition by using reflective flakes, and they determined $Po^{(c)}$ for several fixed Reynolds numbers. Lin *et al.* [20] systematically investigated the critical parameters at which steady flow transits to unsteady flow by direct numerical simulations (DNS). In addition, they derived, on the basis of the theoretical estimation of the growth rate of CSI, the Re dependence of $Po^{(c)}$ as $Po^{(c)} \sim Re^{-4/5}$. Independently, Kida [32] showed the same scaling based on an analytical solution [26]. This scaling is consistent with results obtained by flow visualization [11] and DNS [20]. Incidentally, before the proposal of CSI, the DNS by Lorenzani and Tilgner [30] suggested that the instability growing in a precessing spherical shell can be observed in a spheroidal shell. It is also worth mentioning that Cébron *et al.* [33] recently predicted an instability in the Ekman boundary layer of a precessing spherical shell for sufficiently high Reynolds numbers, which was also investigated experimentally by Sous *et al.* [34]. This instability can grow in a precessing sphere and spheroids, although it may have a small impact on the bulk flow.

For precessing spheroids, in contrast, although there have been experimental studies [6,11,35], no systematic comparison with the linear stability analyses has been conducted. The instability of steady flow in the spheroids is more complicated because all three of the instabilities may occur. Furthermore, it is not trivial for spheroidal cavities whether CSI can grow or not. This is because inertial waves in steady flow decay due to reflections on the cavity wall, although Lin *et al.* [20] showed the possibility of the CSI in a spheroid with a very small ellipticity ($\eta = 0.01$) [35] by comparing flow visualization by injected dye to their DNS of flow in a *sphere*. In the present study, we show that the CSI can grow in spheroidal containers, and we reveal the condition for the instability. For this purpose, we have conducted long-time velocity measurements in two precessing spheroids whose ellipticities are $O(0.1)$ and a sphere by using particle image velocimetry (PIV), which is validated by laser Doppler velocimetry (LDV; see the Appendix). The time-series analysis of the acquired data reveals the Re dependence of the critical Poincaré number $Po^{(c)}$. We will show, in the rest of the present paper, that our experiments support the theoretical predictions.

II. THEORETICAL PREDICTION

A. Magnitude of differential rotation

The linear growth rates of the instabilities of steady flow depend strongly on the cavity shape [20,21]. We can understand this fact by considering the circulation (its uniform angular velocity is denoted by ω) of the fluid about an axis slightly inclined from the spin axis. In other words, a key parameter for the instability of steady flow in a weak precession range is the differential rotation defined by

$$\epsilon = |\hat{\mathbf{z}} - \omega|. \quad (4)$$

Recall that $\hat{\mathbf{z}} = \mathbf{\Omega}_s / \Omega_s$ and the flow is described in the precession frame, in which steady flow is sustained for sufficiently small Po . In the case of a strong spin ($Re \gg 1$) and a weak precession ($Po \ll Re^{-1/2}$), the theory by Busse [36] provides the estimation of the differential rotation in a precessing spheroid. More concretely, the uniform angular velocity of internal flow is given as a

function of Re , Po , and η . In the case in which $\mathbf{\Omega}_s \perp \mathbf{\Omega}_p$, ω is described by

$$\omega = \omega^2 \begin{bmatrix} -\frac{2.62(\omega \text{Re}^{-1})^{1/2} \text{Po}}{2.62^2(\omega/\text{Re}) + [0.259(\omega \text{Re})^{-1/2} + \eta\omega^2]^2} \\ \frac{(0.259(\omega \text{Re})^{-1/2} + \eta\omega^2) \text{Po}}{2.62^2(\omega/\text{Re}) + [0.259(\omega \text{Re})^{-1/2} + \eta\omega^2]^2} \\ 1 \end{bmatrix}. \quad (5)$$

Here, we use the coordinate system shown in Fig. 1(a). In the following arguments, an important quantity is the magnitude ϵ of the differential rotation, which represents the deviation from the solid-body rotational flow, i.e., a flow rotating together with the container. Note that one can easily translate the following arguments into those in terms of the Ekman number Ek , which is often used in geophysics, by replacing Re with Ek^{-1} .

From Eq. (5), we can obtain

$$\epsilon^2 = (1 - \omega^2)^2 + \frac{\omega^4 \text{Po}^2}{2.62^2(\omega/\text{Re}) + [0.259(\omega \text{Re})^{-1/2} + \eta\omega^2]^2}. \quad (6)$$

Let us consider the case in which $\text{Po} \ll 1$, which implies $\omega \approx 1$. Then, Eq. (6) is approximated as

$$\epsilon^2 \approx \frac{\text{Po}^2}{6.93 \text{Re}^{-1} + 0.518 \eta \text{Re}^{-1/2} + \eta^2}. \quad (7)$$

In the following arguments on the scaling, for brevity, η denotes $|\eta|$. We obtain the scaling of ϵ by considering which term dominates in the denominator of the right-hand side of Eq. (7). In the simplest case in which $\eta = 0$ (sphere), we obtain the scaling,

$$\epsilon \sim \text{Po} \text{Re}^{1/2}. \quad (8)$$

On the other hand, for a spheroid with a finite ellipticity, Eq. (7) yields

$$\epsilon \sim \begin{cases} \text{Po} \text{Re}^{1/2} & (\text{Re} \ll 0.14\eta^{-2}), \\ \text{Po} \eta^{-1} & (\text{Re} \gg 200\eta^{-2}), \end{cases} \quad (9a)$$

$$(9b)$$

because the first (third) term in the denominator dominates the other two terms in the former (latter) case. No simple scaling holds in the intermediate Re range, $0.14\eta^{-2} \ll \text{Re} \ll 200\eta^{-2}$. Note that Eq. (9a) is identical to Eq. (8). This implies that spheroids with sufficiently small ellipticity,

$$\eta \ll 0.38 \text{Re}^{-1/2}, \quad (10)$$

can be regarded as a sphere.

B. Growth rates of the three instabilities

As mentioned in the Introduction, the three kinds of instabilities of the steady flow can grow in a precessing spheroid: namely, the shearing and elliptical instabilities [21], which are derived for an inviscid fluid confined in a spheroid, and CSI [20], which may appear in both sphere and spheroid. CSI can grow in a pair of conical shear layers, whose explicit expression was derived by Kida [26]. All of these instabilities stem from a parametric resonance. When a parametric resonance occurs in a rotating fluid, disturbances in the form of inertial modes grow by resonance among them and the background flow with a nonzero azimuthal wave number. Here, the azimuthal wave number is defined with respect to the rotational axis of the fluid. Kerswell [21] analytically derived the growth rates of the shearing and elliptical instabilities, whereas Lin *et al.* [20] estimated the growth rate of

CSI. Their resultant growth rates γ are summarized as

$$\gamma \sim \begin{cases} \epsilon^2 \eta & \text{(elliptic instability),} \\ \epsilon \eta & \text{(shearing instability),} \\ \epsilon \text{Re}^{-1/5} & \text{(CSI).} \end{cases} \quad \begin{array}{l} (11a) \\ (11b) \\ (11c) \end{array}$$

It is seen by comparing Eq. (8) and Eqs. (9a) and (9b) that the differential rotation in a spheroid is much smaller than in a sphere because of the pressure torque on the cavity wall. This means that the asymmetry of a cavity shape stabilizes the steady circulation about the spin axis. Recall that the growth rates (11a) and (11c) are proportional to ϵ for the shearing instability and CSI. This explains why the cavity shape has a significant effect on the stability of steady flow in precessing containers.

C. Critical Poincaré number

We are ready to estimate the critical Poincaré number $\text{Po}^{(c)}$. For a precessing sphere, only CSI grows because $\eta = 0$. Substituting Eq. (8) into Eq. (11c), we obtain

$$\gamma \sim \text{Po} \text{Re}^{3/10}. \quad (12)$$

Thus, considering the balance between this growth rate γ and the viscous decay rate $O(\text{Re}^{-1/2})$ at $\text{Po}^{(c)}$, we obtain the Re dependence of $\text{Po}^{(c)}$ as

$$\text{Po}^{(c)} \sim \text{Re}^{-4/5}. \quad (13)$$

Next we consider the case of precessing spheroids. We assume again that $\text{Po} \ll 1$, and therefore $\epsilon \ll 1$. This implies that the shearing instability always dominates the elliptical instability [see Eqs. (11a) and (11b)]. Comparing Eqs. (11b) and (11c), we can see that when

$$\text{Re} \gtrsim \eta^{-5}, \quad (14)$$

the shearing instability dominates CSI. Conversely, CSI can grow only for $\text{Re} \lesssim \eta^{-5}$.

When $\text{Re} \gg 200\eta^{-2}$ so that Eq. (9b) holds, the linear growth rates of the shearing instability and CSI are

$$\gamma \sim \begin{cases} \text{Po} & \text{(shearing instability),} \\ \text{Po} \eta^{-1} \text{Re}^{-1/5} & \text{(CSI).} \end{cases} \quad \begin{array}{l} (15a) \\ (15b) \end{array}$$

Here, we need to consider whether $200\eta^{-2}$ is larger than η^{-5} or not. When $200\eta^{-2} \lesssim \eta^{-5}$ (i.e., $\eta < 0.17$), the critical Poincaré number, $\text{Po}^{(c)}$, is

$$\text{Po}^{(c)} \sim \text{Re}^{-3/10} \quad (\text{for } 200\eta^{-2} \lesssim \text{Re} \lesssim \eta^{-5}), \quad (16)$$

where CSI grows, and

$$\text{Po}^{(c)} \sim \text{Re}^{-1/2} \quad (\text{for } \eta^{-5} \lesssim \text{Re}), \quad (17)$$

where the shearing instability grows faster than the other. If η is very small, there exists the Reynolds-number range $1 \ll \text{Re} \ll 0.14\eta^{-2}$, which is the range of Re that is smaller than Eq. (16). In this Re range, Eq. (9a) instead of Eq. (9b) holds, and the growth rate of CSI is given by Eq. (12) instead of Eq. (15b). Then, in this small-ellipticity case, the scaling $\text{Po}^{(c)} \sim \text{Re}^{-4/5}$, Eq. (13), which is the same as for CSI in a precessing sphere, holds for $\text{Re} \ll 0.14\eta^{-2}$.

Before closing this section, we briefly consider the case with $\eta \gtrsim 0.17$ (i.e., $200\eta^{-2} \gtrsim \eta^{-5}$). For $\eta \gtrsim 1.9$, $0.14\eta^{-2} \gtrsim \eta^{-5}$, but such a large- η case is beyond the scope of the validity condition of the present analysis. We therefore assume $0.14\eta^{-2} \lesssim \eta^{-5}$. Then a similar analysis leads to $\text{Po}^{(c)} \sim \text{Re}^{-4/5}$ for $\text{Re} \ll 0.14\eta^{-2}$ and $\text{Po}^{(c)} \sim \text{Re}^{-1/2}$ for $\text{Re} \gg 200\eta^{-2}$. However, since Re must be sufficiently large, only the latter scaling may be realized.

In the next section, we show that our experiments support all the theoretical predictions of the scalings (13), (16), and (17).

III. EXPERIMENTS

A. Experimental setup

To realize the precession in the laboratory, we rotate a container filled with degassed water at Ω_s on a turntable rotating at Ω_p . Here, we briefly describe our experiments. Details of our experimental setup are given in our previous papers [11, 16].

We use three kinds of containers with a spherical and a prolate and an oblate spheroidal cavity. The radius of the sphere is $a = 90$ mm. The equatorial and polar radii are $a = 81$ mm and $b = 90$ mm ($\eta = -1/9$) for the prolate spheroid, while $a = 90$ mm and $b = 81$ mm ($\eta = 1/10$) for the oblate spheroid (Fig. 1). These containers, made of acrylic, have a cylindrical outer shape and the spherical or spheroidal cavity (see Fig. 3 of Ref. [11]). We measure the velocity on the equatorial plane [the x - y plane shown in Fig. 1(a)]. The images are taken through the bottom *window* of the cylindrical container so that we can avoid distortion due to the index mismatch of air and the acrylic container.

Note that all measurements are conducted on the turntable, and the measured velocity is on the precessing frame rotating at Ω_p with respect to the laboratory. We emphasize technical difficulties of the PIV on the rotating frame. The electricity of the motor for the spin, a digital camera (Ditect HAS-220), and a computer is supplied through a slip ring. A heavy laser device is set in the laboratory, and a laser beam is guided to run along the precession axis (the rotational axis of the turntable) and converted into the laser sheet on the equatorial plane by a cylindrical lens set on the turntable. This method visualizes flow on the equatorial plane in spite of the turntable rotation at Ω_p , although the accurate alignment of the light beam along the precession axis is required. We have verified the accuracy of the measured velocity fields of flow in the precessing sphere comparing them with DNS under the same condition [11].

The main purpose of the present study is to accurately determine the critical Poincaré number $Po^{(c)}$. For this purpose, we have taken care of the following points. (i) We precisely drive the two rotations by using stepper motors with small step angles (0.036 degrees for Ω_s and 0.072 degrees for Ω_p) and accurate pulse generators. This ensures the high precision of $Po (= \Omega_p/\Omega_s)$. (ii) We accurately control the temperature of the working fluid. We have surrounded the space around the apparatus by insulators and installed an air conditioner for the small space so that the fluid temperature is controlled at $20^\circ\text{C} \pm 0.1^\circ\text{C}$ during long-time (i.e., several hours) experiments. Therefore, the variation of Re , due to the variation of ν , is within $\pm 0.15\%$. (iii) We wait a sufficiently long time to capture the slow growth of an instability. In the experiments, we repeat the measurements by changing Po . Since the growth rate of an instability can be very small when Po is slightly larger than $Po^{(c)}$, we wait for at least $1000T_s$, where $T_s = 2\pi/\Omega_s$ denotes the spin period, after we set a parameter Po . Then, we conduct measurements for the duration of $500T_s$. In general, by means of PIV, we can measure two-dimensional velocity fields. In the present experiments, however, we restrict the area of our measurement plane and measure fluid velocity at a single point, $(x, y, z) = (0, 37, 0)$ mm, so that we can acquire a sufficiently long-time series of the velocity at the point. The frame rate of the digital camera is set in the range between 50 and 400 fps depending on Ω_s . These careful measurements enable us to accurately estimate the power spectrum, based on which we can precisely determine the critical value $Po^{(c)}$ of the Poincaré number.

B. Power spectrum

The power spectrum is defined by

$$P(f) = \frac{\tilde{u}(f)\tilde{u}^*(f)}{T} \quad (18)$$

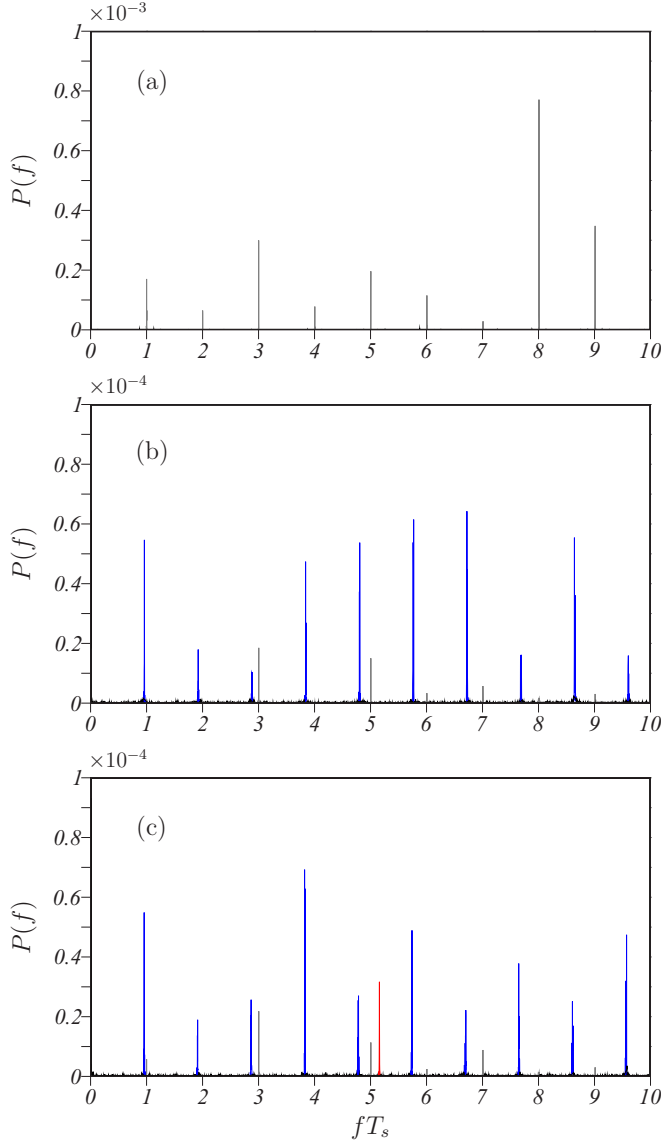


FIG. 2. Power spectrum of (a) solid-body rotational flow ($Po = 0$), (b) steady flow ($Po = 0.0046$), and (c) unsteady flow ($Po = 0.0048$) in the precessing sphere ($Re = 4.0 \times 10^4$). The frequency is normalized by spin period T_s . Gray and blue peaks represent the steady circulations of the container and fluid, respectively. The red peak observed in (c) corresponds to the unsteady mode.

in terms of the Fourier transform

$$\tilde{u}(f) = \frac{1}{2\pi} \int_0^T u(t) \exp\left(-\frac{2\pi i f t}{T}\right) dt \quad (19)$$

of the measured velocity $u(t)$. Here, T is the measurement time and \tilde{u}^* denotes the complex conjugate of \tilde{u} . Figure 2 shows examples of $P(f)$ of the flow in the precessing sphere for a fixed $Re (= 4.0 \times 10^4)$ and three different values of $Po (= 0, 0.0046, 0.0048)$. As emphasized in the preceding

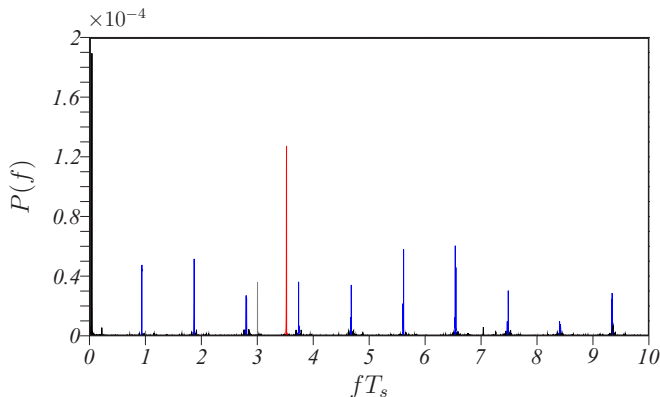


FIG. 3. Power spectrum for an unsteady flow in the oblate spheroid ($\text{Re} = 4.0 \times 10^4$ and $\text{Po} = 0.0425$). Gray and blue peaks represent the steady circulations of the container and fluid, respectively. The red peak corresponds to the unsteady mode.

subsection, we set T to be sufficiently longer than the spin period T_s . Note that the horizontal axis of Fig. 2 is the frequency f normalized by T_s^{-1} .

First, looking at $P(f)$ in Fig. 2(a) for the solid-body rotational flow ($\text{Po} = 0$), we observe the peaks (colored in gray) at $f = nT_s^{-1}$ ($n = 1, 2, \dots$). These peaks are always observed because the container rotates with the period T_s , slightly changing the position of the incident laser sheet for PIV with the same period T_s , and therefore the peaks do not represent any unsteadiness of the flow. Next, looking at $P(f)$ in Fig. 2(b), we notice the other peaks (colored in blue) at $f = 0.96nT_s^{-1}$ in addition to those at $f = nT_s^{-1}$. These peaks are also observed in $P(f)$ of steady flows. Recall that we measure the velocity by PIV, which is based on the images of tracer particles. Since the steady flow is approximately uniform vorticity flow, similar images are taken with the period of the circulation of the internal flow. This is the reason why the spectrum shows the peaks at the frequency $\omega/2\pi$ corresponding to this flow circulation. Therefore, we need to ignore these peaks when we judge the unsteadiness of the flow. Incidentally, we can precisely measure the magnitude ω of the angular velocity of the internal flow (and its period, $1/0.96T_s \approx 1.04T_s$ in this case) which is necessary to estimate the magnitude ϵ of the differential rotation. This is useful to verify the theoretical predictions [36,37] of the differential rotation of steady flows in precessing spheroids, though it is beyond the scope of the present study. In the next subsection, we use this idea by comparing measured values of ω at the critical points with those calculated from Eq. (5). Then, looking at Fig. 2(c) and ignoring the peaks corresponding to the constant rotations of the container and fluid, we notice another peak (colored in red) at $f = 5.16T_s^{-1}$. It is this peak that corresponds to the unstable mode. We can therefore conclude that $\text{Po}^{(c)} \in [0.0046, 0.0048]$ at this Reynolds number ($\text{Re} = 4.0 \times 10^4$) for the sphere.

Figure 3 shows an example of $P(f)$ for the precessing oblate spheroid at the same Reynolds number ($\text{Re} = 4.0 \times 10^4$) as in Fig. 2. Similarly to the case for the sphere, we determine a peak (colored in red) corresponding to the unsteady flow by neglecting the peaks corresponding to the steady circulation of the container and fluid. We notice, however, that there are more peaks than in the case for the sphere (Fig. 2). More specifically, we observe a sharp peak at $f = 0.043T_s^{-1}$ ($= \text{Po}T_s^{-1}$) and we also observe that the peaks corresponding to the flow circulations are accompanied by a pair of lower peaks at $(0.93n \pm \text{Po})T_s^{-1}$. This sharp peak and pairs of lower peaks are irrelevant to the unsteadiness of the flow because they correspond to the rotation Ω_p of the turntable. In our measurements, the location (which should be on the equatorial plane) of the laser sheet oscillates slightly with the period Ω_p on the turntable. This is why we observe the spectral peaks at $fT_s = \text{Po}$ ($= \Omega_p/\Omega_s$). The pairs of lower peaks stem from the same reason. Since the

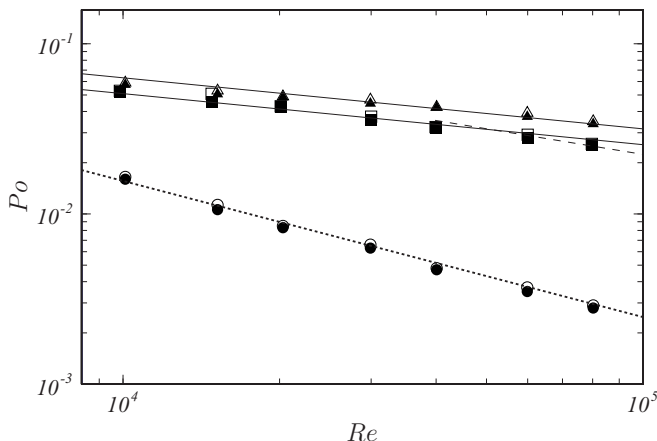


FIG. 4. Flow states in the precessing sphere (circles), prolate spheroid ($\eta = -1/9$, squares), and oblate ($\eta = 1/10$, triangles). Closed and open symbols denote steady and unsteady flows, respectively. Solid, dotted, and dashed lines indicate the scalings $Re^{-3/10}$, $Re^{-4/5}$, and $Re^{-1/2}$, respectively.

values of Po (≈ 0.004) in Figs. 2(b) and 2(c) are much smaller than the value in Fig. 3, the sharp peak at Po and the side peaks are not observed in the former case (Fig. 2). Therefore, we need to ignore these peaks to judge whether an instability grows. Since we observe a peak (colored in red) at $f = 3.52T_s^{-1}$ apart from these spurious peaks, we may conclude that the flow is unsteady. We have verified that the spectrum for a lower Po ($= 0.0422$) does not show such a peak (figure is omitted), and therefore we estimate that the critical Poincaré number $Po^{(c)}$ is in the range $[0.0422, 0.0425]$ for $Re = 4.0 \times 10^4$.

C. Critical Poincaré number

For fixed values of Re in the range $1.0 \times 10^4 \leq Re \leq 8.0 \times 10^4$, by using the procedure described in the preceding subsection for different values of Po , we judge whether the sustained flow for each combination of the parameters (Re, Po) is steady. Then, we determine $Po^{(c)}$ by a bisection method. Since the amplitude of the spectra for the unsteady mode [for example, the red peak in Fig. 2(c)] is affected by noise, it is difficult to determine $Po^{(c)}$ by its extrapolation. However, since we have confirmed that all instabilities observed in the present experiments are supercritical, the bisection method is adequate to determine $Po^{(c)}$. We repeat the bisection for each Re until the increments between the two values of Po for steady and unsteady flows become sufficiently small.

Figure 4 shows the results of the bisections. We denote steady and unsteady flows by closed and open symbols, respectively. Circles, squares, and triangles are the results for the sphere, prolate spheroid ($\eta = -1/9$), and oblate spheroid ($\eta = 1/10$), respectively.

First, looking at the results for the sphere (circles), it is clear that $Po^{(c)}$ is proportional to $Re^{-4/5}$. This is consistent with the theoretical prediction, Eq. (13), derived by Lin *et al.* [20] and Kida [32] as well as DNS [20]. The least-squares method estimates the coefficient of the scaling as $Po^{(c)} = 25 Re^{-4/5}$. We further verify the obtained critical values $Po^{(c)}$ in the Appendix, where we show that the results of flow visualization [11] are in good agreement with the present accurate measurements. We also show in the Appendix that measurements by LDV validate the present PIV results.

The results for the spheroids are also consistent with the theoretical predictions described in Sec. II. Recall that when $Re \lesssim \eta^{-5}$, CSI dominates the shearing instability. Our experiments are within this range ($Re < 10^5$ and $\eta = -1/9, 1/10$). Therefore, the theory predicts the scaling, Eq. (16); namely, $Po^{(c)} \sim Re^{-3/10}$. The triangles (the oblate spheroid, $\eta = 1/10$) and squares (the prolate spheroid, $\eta = -1/9$) in Fig. 4 indeed support this scaling. Although we observe the

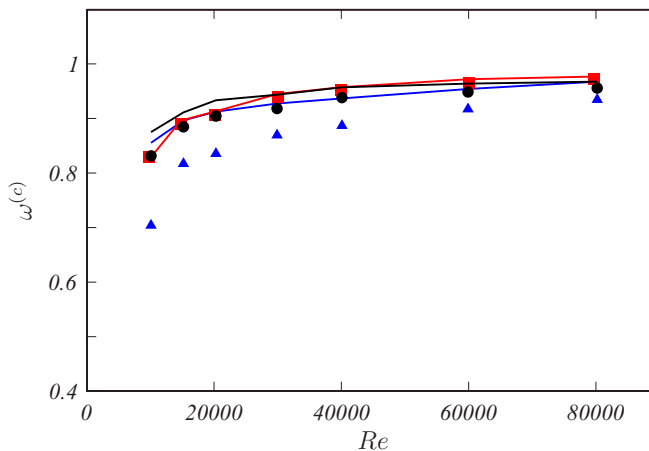


FIG. 5. The magnitude $\omega^{(c)}$ of the angular velocity of the approximately uniform vorticity flow at the critical point $\text{Po} = \text{Po}^{(c)}$. Lines (black, the sphere; red, the prolate spheroid; blue, the oblate spheroid) are the estimation on the basis of the spectral peaks (such as the blue peaks in Figs. 2 and 3). Symbols (\bullet , the sphere; \blacksquare , the prolate spheroid; \blacktriangle , the oblate spheroid) are the theoretical predictions by Eq. (5).

deviation from the scaling in a lower Re range, this is also explained by the theory because the scaling is valid under the assumption $\text{Re} \gg 200\eta^{-2}$ ($\approx 2 \times 10^4$ for $\eta \approx 0.1$) for the scaling (9b) of the differential rotation to hold. In this range of Re , the experimental results are fitted as $\text{Po}^{(c)} = 1.0\text{Re}^{-3/10}$ (for the oblate spheroid) and $0.81\text{Re}^{-3/10}$ (for the prolate spheroid), respectively. Furthermore, for the prolate spheroid, we observe a small deviation from the scaling, and it seems to approach another scaling with a larger (in magnitude) exponent. This is also consistent with the theories. We expect $\text{Po}^{(c)} \sim \text{Re}^{-1/2}$, Eq. (17), in a higher Reynolds-number range ($\text{Re} \gtrsim \eta^{-5} \approx 6 \times 10^4$ for the prolate spheroid and 10^5 for the oblate spheroid) because the shearing instability grows faster than CSI.

The most important observation in Fig. 4 is that, for a given Re , the instability grows with much lower Po in the precessing sphere than in the spheroids. This is explained in terms of the magnitude ϵ of the differential rotation. Recall that the growth rate (11c) increases with ϵ . As discussed in the last paragraph of Sec. II B, because of the absence of the pressure torque in a sphere, the differential rotation, at a given combination of Re and Po , is much larger for a sphere ($\eta = 0$). This explains why the CSI grows with significantly lower Po in a sphere.

To further examine the consistency between the present experiments and the theory, here we estimate the magnitude $\epsilon^{(c)}$ of the differential rotation at the critical points. Since we need to use Eq. (5) for this purpose, we first verify it. As mentioned in Sec. III B, the peaks (such as the blue peaks in Figs. 2 and 3) of $P(f)$ contain the information of the approximately uniform circulation of the fluid. More concretely, we use the fact that the blue peaks in Figs. 2 and 3 correspond to the frequency $\omega/2\pi$ of the approximately uniform vorticity flow. We plot by solid lines in Fig. 5 the value of $\omega^{(c)}$ measured from the peaks. On the other hand, we substitute the parameters η , Re , and $\text{Po}^{(c)}$ into Eq. (5) to obtain, by the Newton method, the theoretical prediction of $\omega^{(c)}$ at the critical point. Figure 5 shows that, although the theory underestimates $\omega^{(c)}$ for the oblate spheroid, the theoretical prediction is in excellent (almost perfect for the prolate spheroid) agreement with the measurements. Incidentally, it is interesting to observe that $\omega^{(c)}$ is approximately independent of the ellipticity.

Then, we further substitute $\omega^{(c)}$, for which we use the theoretical values for consistency, into Eq. (6) to obtain the magnitude $\epsilon^{(c)}$ of the differential rotation at the critical points. Thus estimated values of $\epsilon^{(c)}$ are plotted as functions of Re in Fig. 6. It is clear that, irrespective of the ellipticity (including $\eta = 0$ for the sphere), $\epsilon^{(c)}$ is proportional to $\text{Re}^{-3/10}$, though we observe deviation from

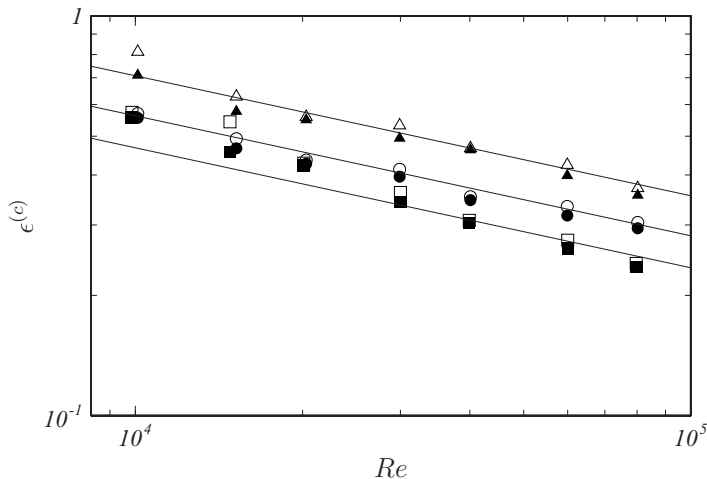


FIG. 6. The magnitude $\epsilon^{(c)}$ of the differential rotation at the critical point $Po = Po^{(c)}$. Symbols are the same as in Fig. 4. Solid lines indicate the scaling $\epsilon^{(c)} \sim Re^{-3/10}$.

the scaling in the low-Re range for the prolate spheroid. Recall that the growth rate of CSI scales as $\gamma \sim \epsilon Re^{-1/5}$; see Eq. (11c). At the critical points, this must be balanced with the viscous decay rate, i.e., $\gamma \sim Re^{-1/2}$, and $\epsilon^{(c)}$ is proportional to $Re^{-3/10}$. The scaling observed in Fig. 6, therefore, implies that the instability in this range of Re and for these η is CSI. Incidentally, the Ekman-boundary-layer instability, which may occur for $Re \gtrsim 10^5$, leads to $\epsilon^{(c)} \sim Re^{-1/2}$ [33]. Although our experimental setup cannot reach the regime, it is interesting to investigate the impact of the boundary-layer instability on the bulk flow in the high Re regime.

IV. CONCLUSION

We have conducted well-controlled laboratory experiments (Sec. III) to investigate the instability of steady flow sustained in a slowly precessing sphere and spheroids. We have measured, by PIV, a long-time series of a velocity component at a point on the equatorial plane and analyzed its power spectrum (examples are shown in Figs. 2 and 3) to judge the steadiness of the flow. Then, we have accurately determined using a bisection method the critical Poincaré number $Po^{(c)}$ (Fig. 4) for each Reynolds number Re , which is the reciprocal of the Ekman number, for three different containers (sphere, prolate spheroid with $\eta = -1/9$, and oblate spheroid with $\eta = 1/10$). In the Reynolds-number range $1.0 \times 10^4 \leq Re \leq 8.0 \times 10^4$, $Po^{(c)}$ for the sphere scales as $Po^{(c)} = 25 Re^{-4/5}$ (circles in Fig. 4). This result is consistent with the theoretical prediction, Eq. (13), by Lin *et al.* [20] and Kida [32], DNS [20], and the flow visualization [11], which is evidence that the conical shear-driven parametric instability (CSI) grows in the sphere. Furthermore, we have shown that for the spheroids with the ellipticity $\eta = O(0.1)$, $Po^{(c)} \propto Re^{-3/10}$ in this Re range; see the triangles and squares in Fig. 4. The least-squares method estimates the coefficient to be 1.0 and 0.81 for the oblate and prolate spheroids, respectively. These results are also consistent with the theoretical prediction, Eq. (16), and they imply that the instability is CSI. In other words, for small η , in the Re range $Re \lesssim \eta^{-5}$, CSI dominates the shearing instability. It is interesting that the peaks of the spectra (such as the blue peaks in Figs. 2 and 3), which stem from the nature of the PIV, enable us to estimate the magnitude ω of the angular velocity of the circulation of the steady or weakly unsteady internal flow. The estimations are in good agreement with the theory (Fig. 5). Then, using these values of ω at the critical points, we have evaluated the magnitude $\epsilon^{(c)}$ of the differential rotation (Fig. 6) at the critical points. The results show that $\epsilon^{(c)}$ is proportional to $Re^{-3/10}$ irrespective of the container's

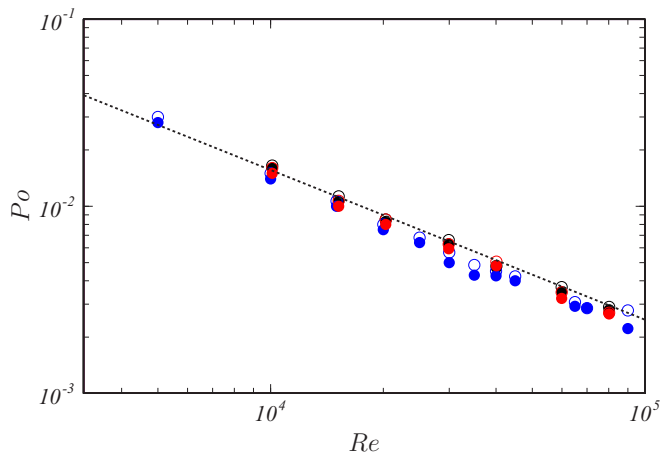


FIG. 7. Flow states in the precessing sphere. Closed and open circles denote steady and unsteady flows, respectively. The results were obtained by PIV (black), LDV (red), and visualizations (blue). The dotted line is the same as that in Fig. 4, which is proportional to $Re^{-4/5}$.

shape. This result is also consistent with the growth rate (11c) of CSI, and further supports the conclusion that CSI grows in the three containers in this Re range.

Although our experimental apparatus restricts the Reynolds number to be less than 10^5 , the theory described in Sec. II predicts that the shearing instability can grow in our spheroidal containers ($\eta \approx 0.1$) for $Re \gtrsim 10^5$ to observe the scaling of $Po^{(c)}$ proportional to $Re^{-1/2}$. Furthermore, if we use spheroids with a much smaller η and conduct experiments for a wider Re range, then the three scalings $Po^{(c)} \sim Re^{-4/5}$, $Re^{-3/10}$, and $Re^{-1/2}$ can be observed successively as Re increases. These experiments as well as DNS, showing direct evidence that CSI grows in precessing spheroids, will form the basis of important future studies.

ACKNOWLEDGMENT

This study was partly supported by a JSPS Grant-in-Aid for Scientific Research (16H04268).

APPENDIX: COMPARISON WITH OTHER EXPERIMENTAL TECHNIQUES

As we described in Sec. III, we carefully conduct PIV. In this Appendix, we validate the results with those obtained by other methods. First, we compare in Fig. 7 the PIV results (black symbols) with those with flow visualizations (blue symbols) [11]. Only the case for the precessing sphere is shown. We visualize the flow by using reflective flakes, and we judge the steadiness of the flow by the steadiness of the visualized pattern [38]. This simple technique yields results in good agreement with the present accurate measurements. Although there are small quantitative deviations, the visualization leads to the same scalings of $Po^{(c)}$. However, for the spheroid (in particular, the oblate spheroid), the stationary pattern is very obscure and we could not use the flow visualization to determine the critical Poincaré number.

Next, we compare the present results for the sphere with those by LDV (Dantec Dynamics FlowExplorer). Since the signal analyzer of the LDV system is too large to set on the turntable, we set it in the laboratory and only the head rotates together with the turntable. Through a photocoupler set on the axis of the turntable, the light signal received by the head on the turntable is transferred to the signal analyzer in the laboratory. We analyze the time-series of velocity components at a single point to judge the steadiness of the flow. Although the time increments of measured velocity are irregular and therefore we need a special treatment for the spectral analysis, the LDV can easily

acquire a long-time (say, $2000T_s$) data. Then, using the bisection method, we determined $Po^{(c)}$, which is plotted with red symbols in Fig. 7. The obtained values are consistent with the PIV results (black symbols). For example, for $Re = 2.03 \times 10^4$, the PIV concludes $0.0083 < Po^{(c)} < 0.0085$, whereas the LDV leads to $0.008 < Po^{(c)} < 0.0085$. However, although the LDV is more appropriate for the time-series analysis, we encountered difficulty in measuring the velocity of the flow in the spheroids. As mentioned in Sec. III, we use an acrylic cylindrical container with a spheroidal cavity, and we measure the velocity from the bottom of the cylinder (see Fig. 3 of Ref. [11]). Thanks to this technique, we can avoid the refraction due to the index mismatch of the acrylic container and air. This is sufficient for the accurate PIV. However, for LDV we need to detect weak scattered light, and the refraction on the cavity wall (i.e., the curved boundary between the acrylic container and water) is not negligible. Therefore, we have to carefully set the alignment of incident beams for the LDV. This is possible in principle, but the setup for PIV is much easier and PIV is equally accurate. Therefore, in the present study we have conducted the measurements by PIV rather than LDV.

-
- [1] M. Le Bars, D. Cébron, and P. Le Gal, Flows driven by libration, precession, and tides, *Annu. Rev. Fluid Mech.* **47**, 163 (2015).
 - [2] W. V. R. Malkus, Precession of the earth as the cause of geomagnetism, *Science* **160**, 259 (1968).
 - [3] J. J. Kobine, Azimuthal flow associated with inertial wave resonance in a precessing cylinder, *J. Fluid Mech.* **319**, 387 (1996).
 - [4] R. Manasseh, Nonlinear behaviour of contained inertia waves, *J. Fluid Mech.* **315**, 151 (1996).
 - [5] J. P. Vanyo and J. R. Dunn, Core precession: Flow structures and energy, *Geophys. J. Int.* **142**, 409 (2000).
 - [6] J. Noir, P. Cardin, D. Jault, and J.-P. Masson, Experimental evidence of nonlinear resonance effects between retrograde precession and the tilt-over mode within a spheroid, *Geophys. J. Int.* **154**, 407 (2003).
 - [7] S. Goto, N. Ishii, S. Kida, and M. Nishioka, Turbulence generator using a precessing sphere, *Phys. Fluids* **19**, 061705 (2007).
 - [8] A. Tilgner, Kinematic dynamos with precession driven flow in a sphere, *Geophys. Astrophys. Fluid Dyn.* **101**, 1 (2007).
 - [9] R. Lagrange, C. Eloy, F. Nadal, and P. Meunier, Instability of a fluid inside a precessing cylinder, *Phys. Fluids* **20**, 081701 (2008).
 - [10] S. Kida and M. Shimizu, A turbulent ring and dynamo in a precessing sphere, *J. Phys.: Conf. Ser.* **318**, 072031 (2011).
 - [11] S. Goto, A. Matsunaga, M. Fujiwara, M. Nishioka, S. Kida, M. Yamato, and S. Tsuda, Turbulence driven by precession in spherical and slightly elongated spheroidal cavities, *Phys. Fluids* **26**, 055107 (2014).
 - [12] S. Goto, M. Shimizu, and G. Kawahara, Turbulent mixing in a precessing sphere, *Phys. Fluids* **26**, 115106 (2014).
 - [13] J. Hœrault, T. Gundrum, A. Giesecke, and F. Stefani, Subcritical transition to turbulence of a precessing flow in a cylindrical vessel, *Phys. Fluids* **27**, 124102 (2015).
 - [14] L. Cappanera, J.-L. Guermond, J. Léorat, and C. Nore, Two spinning ways for precession dynamo, *Phys. Rev. E* **93**, 043113 (2016).
 - [15] Y. Lin, P. Marti, J. Noir, and A. Jackshon, Precession-driven dynamos in a full sphere and the role of large scale cyclonic vortices, *Phys. Fluids* **28**, 066601 (2016).
 - [16] Y. Horimoto and S. Goto, Sustaining mechanism of small-scale turbulent eddies in a precessing sphere, *Phys. Rev. Fluids* **2**, 114603 (2017).
 - [17] Y. Horimoto, G. Simonet-Davin, A. Katayama, and S. Goto, Impact of a small ellipticity on the sustainability condition of developed turbulence in a precessing spheroid, *Phys. Rev. Fluids* **3**, 044603 (2018).
 - [18] K. S. Reddy and M. Le Bars, Turbulent kinematic dynamos in ellipsoids driven by mechanical forcing, *Geophys. Res. Lett.* **45**, 1741 (2018).

- [19] K. Komoda and S. Goto, Three-dimensional flow structures of turbulence in precessing spheroids, *Phys. Rev. Fluids* **4**, 014603 (2019).
- [20] Y. Lin, P. Marti, and J. Noir, Shear-driven parametric instability in a precessing sphere, *Phys. Fluids* **27**, 046601 (2015).
- [21] R. R. Kerswell, The instability of precession flow, *Geophys. Astrophys. Fluid Dyn.* **72**, 107 (1993).
- [22] R. R. Kerswell, Elliptical instability, *Annu. Rev. Fluid Mech.* **34**, 83 (2002).
- [23] H. Bondi and R. A. Lyttleton, On the dynamical theory of the rotation of the earth. II. The effect of precession on the motion of the liquid core, *Math. Proc. Cambridge Philos. Soc.* **49**, 498 (1953).
- [24] K. Stewartson and P. H. Roberts, On the motion of a liquid in a spheroidal cavity of a precessing rigid body, *J. Fluid Mech.* **17**, 1 (1963).
- [25] R. R. Kerswell, On the inertial shear layer spawned by critical regions in oscillatory Ekman boundary layers, *J. Fluid Mech.* **298**, 311 (1995).
- [26] S. Kida, Steady flow in a rapidly rotating sphere with weak precession, *J. Fluid Mech.* **680**, 150 (2011).
- [27] R. Hollerbach and R. R. Kerswell, Oscillatory internal shear layers in rotating and precessing flows, *J. Fluid Mech.* **298**, 327 (1995).
- [28] A. Tilgner, Magnetohydrodynamics flow in precessing spherical shells, *J. Fluid Mech.* **379**, 303 (1999).
- [29] A. Tilgner, Non-axisymmetric shear layers in precessing fluid ellipsoidal shells, *Geophys. J. Int.* **136**, 629 (1999).
- [30] S. Lorenzani and A. Tilgner, Fluid instabilities in precessing spheroidal cavities, *J. Fluid Mech.* **447**, 111 (2001).
- [31] J. Noir, D. Jault, and P. Cardin, Numerical study of the motions within a slowly precessing sphere at low Ekman number, *J. Fluid Mech.* **437**, 283 (2001).
- [32] S. Kida, Instability by weak precession of the flow in a rotating sphere, *Proc. IUTAM* **7**, 183 (2013).
- [33] D. Cébron, R. Laguerre, J. Noir, and N. Schaeffer, Precessing spherical shells: Flows, dissipation, dynamo and the lunar core, *Geophys. J. Int.* **219**, S34 (2019).
- [34] D. Sous, J. Sommeria, and D. Boyer, Friction law and turbulent properties in a laboratory Ekman layer, *Phys. Fluids* **25**, 046602 (2013).
- [35] J. Vanyo, P. Wilde, P. Cardin, and P. Olson, Experiments on precessing flows in the earth's liquid core, *Geophys. J. Int.* **121**, 136 (1995).
- [36] F. H. Busse, Steady fluid flow in a precessing spheroidal shell, *J. Fluid Mech.* **33**, 739 (1968).
- [37] S. Kida, Steady flow in a rapidly rotating spheroid with weak precession: I, *Fluid Dyn. Res.* **52**, 015513 (2020).
- [38] S. Goto, S. Kida, and S. Fujiwara, Flow visualization using reflective flakes, *J. Fluid Mech.* **683**, 417 (2011).